Transient Rheology of the Uppermost Mantle Beneath the Mojave Desert, California

Fred F. Pollitz

U.S. Geological Survey
345 Middlefield Rd., MS 977
Menlo Park, CA 94025
U.S.A.

Earth and Planetary Science Letters
Vol. 215/1-2, pp. 89-104
September, 2003

Abstract. Geodetic data indicate that the M7.1 Hector Mine, California earthquake was followed by a brief period (a few weeks) of rapid deformation preceding a prolonged phase of slower deformation. We find that the signal contained in continuous and campaign GPS data for 2.5 years after the earthquake may be explained with a transient rheology. Quantitative modeling of these data with allowance for transient (linear biviscous) rheology in the lower crust and upper mantle demonstrates that transient rheology in the upper mantle is dominant, its material properties being characterized by two characteristic relaxation times ~0.07 and ~2 years. The inferred mantle rheology is a Jeffreys solid in which the transient and steady state shear moduli are equal. Consideration of a simpler viscoelastic model with a linear univiscous rheology (2 fewer parameters than a biviscous model) shows that it consistently underpredicts the amplitude of the first ~3 months signal, and allowance for a biviscous rheology is significant at the 99.0% confidence level. Another alternative model -- deep postseismic afterslip beneath the coseismic rupture -- predicts a vertical velocity pattern opposite to the observed pattern at all time periods considered. Despite its plausibility, the advocated biviscous rheology model is non-unique and should be regarded as a viable alternative to the nonlinear mantle rheology model for governing postseismic flow beneath the Mojave Desert.

1 Introduction

The rheology of the lithosphere and asthenosphere is of central importance for understanding the evolution of plate boundary zones, the role of crust-mantle coupling in driving continental deformation, and predicting the response of the lithosphere to glacial and lacustrine loads as well as earthquakes. In turn, the study of this response is the principal way in which the rheology of the deep subsurface is inferred.

The rheology of the bulk Earth is generally represented in terms of the depth-dependent distribution of its viscoelastic structure [1]. At timescales of $\sim 10^6$ years this is based on the correlation of the long wavelength geoid with Earth's interior convective flow pattern constrained by the surface kinematics (e.g., [2,3]). Generation of surface and subsurface topography over geologic time also provides a window into the flow of the lower crust and uppermost mantle, yielding estimates of the viscosities of these regions [4]. At timescales of several thousand years and wavelengths of 100s to 1000s of km, most constraints on rheology are provided by postglacial rebound data

(e.g., summaries by [1] and [5]), yielding estimates of the elastic plate thickness and upper and lower mantle viscosity structure. At timescales of several months to several decades and wavelengths of <1000 km, geodetic observations of postseismic relaxation following major (magnitude ~>7) earthquakes (e.g., [6–14] among many others) allow estimation of elastic plate thickness and lower crust and upper mantle viscosities.

The focus of this paper is the viscoelastic structure of the lower crust and uppermost mantle. Postseismic crustal deformation measurements provide the greatest wealth of data bearing on the rheology of these regions. Experience has shown that such data is often difficult to interpret unambiguously owing to the similar ground deformation predicted by different postseismic flow mechanisms, notably afterslip and bulk viscoelastic relaxation [15–19]. When viscoelastic mechanisms can be satisfactorily discriminated from other candidate processes, one further needs to reckon with the constitutive relation between stress and strain since it is fundamental in controlling the viscoelastic response of the lower crust and mantle. The rheology of these regions is almost certainly more complicated than that of a simple Maxwell viscoelastic solid which is usually adopted in deformation modeling studies. Rocks in the laboratory generally exhibit a nonlinear response to stress over a broad range of frequencies [20,21]. At seismic frequencies, attenuation phenomena are well explained with an absorption band model [21] involving relaxation over a continuum of frequencies ranging from about 0.001 Hz to 10 Hz. This behavior may be roughly approximated as that of a homogeneous standard linear solid Earth of viscosity $\sim 10^{16}$ Pa s [22]. This is well below the value of $\sim 10^{19}$ Pa s deduced in most postseismic relaxation studies, but almost all of these studies have assumed a Maxwell rheology. It has been previously remarked [22] that postglacial rebound takes place on a timescale that is sensitive to both anelastic and viscous deformation mechanisms in the Earth. The question arises as to whether the mechanisms that control both seismic wave attenuation and long term viscous deformation also play a role in postseismic deformation and, if so, whether postseismic deformation observations can capture the transition between the two deformation modes.

At the small strains and timescales involved in seismic wave attenuation and postseismic relaxation, a transient response is expected [21]. Recent studies which focus on the earliest postseismic response yield effective viscosities of order 10^{17} Pa s [15,23], and an explanation involving a transient rheology comes to the forefront. The

large strain rates observed in the epicentral region of the 1992 Landers earthquake during the first three months postseismic period [16], in contrast with the post-three month period, have been interpreted by Ivins [23] as the response of heterogeneous lower crust which, in terms of composite media theory, is best described as a transient rheology represented by a Burghers body. Further evidence suggestive of a transient rheology is provided by postseismic deformation observed by GPS and InSAR in the 9 months after the M7.1 1999 Hector Mine earthquake (Figure 2). Pollitz et al. [15] inferred a relaxing mantle source of the postseismic deformation and proposed that the effective mantle viscosity increased with time from $\sim 5\times10^{17}$ Pa s in the first few months to $\sim 2\times10^{19}$ Pa s between 3 months and 3 years after the respective earthquakes. Such a trend with time can plausibly arise with either a nonlinear [15,24] or a transient rheology.

In this paper we consider in greater detail the implications of post-Hector Mine deformation measurements and address whether or not these measurements can be explained with a transient rheology. It is likely possible, in principle, to interpret available postseismic deformation data in terms of a transient rheology that merges the behavior of the absorption model at short time scale and viscous behavior at long time scale (i.e., [22]). Here we seek an interpretation of this data with the simplest realization of a transient rheology -- a Burghers body (Figure 1). For shear deformation, the constitutive equation governing a Burghers body is [25]

$$2\eta_2\ddot{\varepsilon} + 2\mu_2\dot{\varepsilon} = \frac{\eta_2}{\mu_1}\,\ddot{\sigma} + \left[1 + \frac{\mu_2}{\mu_1} + \frac{\eta_2}{\eta_1}\right]\dot{\sigma} + \frac{\mu_2}{\eta_1}\,\sigma \qquad (1)$$

where η_1, μ_1 are steady state viscosity and shear modulus, respectively, and η_2, μ_2 are the transient viscosity and transient shear modulus, respectively (Figure 1). For a constant stress load σ_0, the strain response is given by

$$\varepsilon = \frac{\sigma_0}{2\mu_1} + \frac{\sigma_0}{2\mu_2}\left[1 - \exp(-t\,/\,\tau_2)\right] + \frac{\sigma_0}{2\mu_1}\frac{t}{\tau_1} \qquad (2)$$

where $\tau_1 = \eta_1 / \mu_1$ and $\tau_2 = \eta_2 / \mu_2$. The response to an imposed constant stress step is thus a superposition of three effects: The instantaneous elastic response, an exponentially-decaying transient response, and a linearly-increasing steady-state response. The transient and steady-state responses are associated with relaxation times τ_2 and τ_1, respectively. If $\tau_2 \ll \tau_1$, then the transient response will be relatively rapid and distinguishable from the steady-state response. If existing postseismic

observations are interpreted with this material, then the rapid early response is associated with the short "transient" characteristic relaxation time of the Kelvin element of the solid -- τ_2, whereas the slower later response is controlled by the longer "steady" characteristic relaxation time of the Maxwell element of the solid -- τ_1 (Figure 1).

We shall make use of three-component GPS data covering the period from 10 days to 2.5 years after the Hector Mine earthquake. This samples both the very early, rapid and later, relatively slow postseismic deformation phases. Although earlier observations are available, we do not make use of deformation data from the first 10 days postseismic period in order to avoid the possible influence of aftershocks [26]. We find that the GPS time series contain signals sensitive to both crust and mantle relaxation, and in the framework of linear viscoelasticity theory, they are most consistent with a transient rheology of the mantle characterized by two distinct relaxation times.

2 Postseismic GPS Observations

We employ three-component continuous GPS data provided by the Southern California Integrated GPS Network (SCIGN) [27] and campaign GPS data provided by the US Geological Survey (USGS) [28]. The locations of these sites are shown in Figure 2. Sixteen of the 29 sites are SCIGN sites; 13 sites are USGS campaign sites with varying levels of campaign sampling. There are a total of 47526 time samples from 135 time series employed in this analysis.

The time series for the SCIGN sites have been processed in network mode using GAMIT/GLOBK software in a fixed North America reference frame defined by 4 IGS fiducial sites tightly constrained to ITRF96, then rotated to a regional reference frame designed to match a known set of 30 SCIGN station coordinates and velocities in southern California [29]. The time series for the 13 USGS sites have been augmented by a subset of SCIGN data for the other 16 sites at times corresponding to the observation times of the campaign sites. The 29 collective sites were then processed in network mode using GYPSY software in a fixed North America reference frame defined by 13 ITRF97 fiducial stations [30]. This allows estimation of velocities at the 13 USGS campaign sites in a reference frame that is easily related to the reference frame of the SCIGN network processing. The difference between the two reference frames is

well described as the difference between two velocity shift vectors, obtained for each network separately as described in section 3.1.

The vertical time series are particularly susceptible to annual and semi-annual variations likely arising from seasonal pressure fluctuations [31]. In order to remove this signal, I estimate four sinusoidal components (equivalent to the amplitude and phase of the annual and semi-annual signals) simultaneously with velocity and initial position, then subtract the determined sinusoidal components from the vertical time series. Typical amplitude of the annual and semi-annual terms are about 1–2 mm.

One of the sites, OAES (Figure 2) is found to exhibit a sharp acceleration in motion towards the south about 2 years after the Hector Mine earthquake in the SCIGN data time series. We attribute this to local deformation sources unrelated to postseismic relaxation from the Hector Mine earthquake. For this reason we exclude data from this site in our evaluation of candidate viscoelastic models.

Time series are shown in Figure 3a for three selected SCIGN sites and in Figure 3b for three selected USGS sites for the first 2.5 years; Figures 3c and 3d show the same time series for the first 0.25 years. A pronounced curvature with time is apparent, suggesting that more than one time signal (i.e., a superposition of a steady state signal and exponentially-decaying signals) is present. These time series reveal that the first ~0.2 year postseismic period is generally associated with much faster deformation rates than at later times. The chief characteristics of this "transient relaxation" period are its rapidity and its ubiquitous presence throughout the considered networks, suggesting a common underlying broadscale physical process. In general, the SCIGN network observations provide the densely sampled time-dependent signals critical to detecting both potential transient and steady state signals. The observations provided by the USGS network are less dense in time but more dense in space, especially helping cover the area near the 1992 Landers rupture. With both data sets the use of vertical in addition to horizontal components provides vital information on the relative contributions of crust and mantle relaxation.

3 Modeling of postseismic deformation

3.1 Representation of postseismic deformation

Following [15], we interpret the GPS time series as a superposition of two distinct processes: (1) steady tectonic loading and (2) viscoelastic relaxation of the lower crust and upper mantle. We model three-dimensional displacement $\mathbf{u}(\hat{\mathbf{r}}_i, t)$ at GPS site $\hat{\mathbf{r}}_i$ at Earth's surface and time t after the earthquake as:

$$\mathbf{u}(\hat{\mathbf{r}}_i, t) = \mathbf{v}_{\text{def}}(\hat{\mathbf{r}}_i, t) + \mathbf{v}_{\text{load}}(\hat{\mathbf{r}}_i)t + \mathbf{a}_i + \mathbf{b}t \tag{3}$$

where $\mathbf{v}_{\text{def}}$ and $\mathbf{v}_{\text{load}}$ are the contributions of viscoelastic relaxation and steady tectonic loading, respectively, the $\{\mathbf{a}_i\}$ are constant station vector offsets, and $\mathbf{b}$ is a common mode velocity shift of the regional reference frame employed in the GPS analysis with respect to the epicentral region of the earthquake. Since $\mathbf{v}_{\text{def}}(\hat{\mathbf{r}}_i, t) = 0$ at $t=0$, the $\{\mathbf{a}_i\}$ would be zero given perfect observations. However, given the fact that observations are imperfect and, especially, that many time series in the data sets begin much later than the immediate postseismic period (several SCIGN sites used in the present study were emplaced > 2 months after the earthquake), it is necessary to introduce these station offsets.

In practice, both $\mathbf{a}_i$ and $\mathbf{b}$ for a given deformation component $\mathbf{v}_{\text{def}}$ are determined separately for each GPS network (SCIGN and USGS) by fitting the theoretical displacement $\mathbf{u}(\hat{\mathbf{r}}_i, t)$ to the observed time series $\mathbf{u}_{\text{obs}}(\hat{\mathbf{r}}_i, t_{ij})$, where t_{ij} are the available observation times at site i. Specifically we minimize the following misfit functions for the three Cartesian indices k=1,2,3:

$$\chi^2{}_k = \sum_i \sum_j \frac{\left[\hat{\mathbf{x}}_k(\hat{\mathbf{r}}_i)\cdot\mathbf{u}(\hat{\mathbf{r}}_i, t_{ij}) - \hat{\mathbf{x}}_k(\hat{\mathbf{r}}_i)\cdot\mathbf{u}_{\text{obs}}(\hat{\mathbf{r}}_i, t_{ij})\right]^2}{\left[\sigma_{ijk}\right]^2} \tag{4}$$

where $\hat{\mathbf{x}}_k(\hat{\mathbf{r}}_i)$ is the local unit vector at $\hat{\mathbf{r}}_i$ on the spherical Earth pointing in the due East (k=1), North (k=2), and up (k=3) directions, respectively, and σ_{ijk} is the standard deviation of the k–direction measurement at site i and time t_{ij}. Thus, given sets of time series from two station networks, we minimize six misfit functions in order to obtain two sets $\{\mathbf{a}_i, \mathbf{b}\}$, one set for each network. This involves three inversions for 17 parameters (16 $\hat{\mathbf{x}}_k\cdot\mathbf{a}_i$ and $\hat{\mathbf{x}}_k\cdot\mathbf{b}$) using SCIGN data and three inversions for 30 parameters (29 $\hat{\mathbf{x}}_k\cdot\mathbf{a}_i$ and $\hat{\mathbf{x}}_k\cdot\mathbf{b}$) using USGS data. We assume no steady state com-

ponent for the vertical data, so that $\hat{\mathbf{x}}_3 \cdot \mathbf{b} = 0$ a-priori. A total of $51 + 90 - 2 = 139$ parameters are estimated in this fashion. After propagation of the data errors typical values of $\mathbf{a}_i$ are ~±5 mm with standard errors ~0.1–0.3 mm. The reference frame shift between the two data sets determined by their respective **b**–values is (13.6 ± 0.17 mm/yr, 11.8 ± 0.14 mm/yr) in (East, North) coordinates. Removal of this common mode shift between the SCIGN and USGS networks renders them consistent at the sub-mm/yr level.

The background tectonic loading component $\mathbf{v}_{\text{load}}(\hat{\mathbf{r}}_i)$ is prescribed by a uniform engineering strain rate rate of 0.1 μrad/yr resolved onto a N40˚W trending vertical plane. This value is obtained from several trilateration surveys in the central Mojave Desert prior to 1992 [32], and it is considered a good representation of the pre-Landers velocity field.

The viscoelastic deformation component $\mathbf{v}_{\text{def}}$ depends on the viscoelastic structure and the source models of the major contributing earthquakes -- the 1992 Landers and 1999 Hector Mine earthquakes. We adopt the slip model of [33] for the Landers earthquake and [34] for the Hector Mine earthquake. The viscoelastic structure is parameterized in terms of depth-dependent elastic moduli (bulk and shear modulus) and viscosities in the ductile lower crust and mantle (Figure 4). The lower crust in the viscoelastic model is bounded by the maximum depth extent of regional earthquakes [35] and the Moho depth [36]. For simplicity we assume that both the lower crust and upper mantle are homogeneous.

3.2 Choice of rheology

Many possibilities exist for lower crust and upper mantle viscosity structure that could explain the primary patterns in the GPS observations. For example, if we were to allow both the lower crust and mantle to be a Burghers solid, then in addition to known steady-state elastic parameters in these regions we would need to reckon with 6 additional unknowns -- the transient viscosity, transient shear modulus, and steady state viscosity in both of these regions. In order to limit the range we restrict the possibility of transient rheology to one layer only, i.e., either the lower crust or upper mantle is permitted to have a Burghers body rheology, but the other is assumed Maxwell viscoelastic.

The behavior of a Burghers body (Figure 1) may be represented by its Laplace-transformed shear modulus, which may be derived from equation (1):

$$\mu(s) = \mu_1 s \frac{(s + \tau_2^{-1})}{(s + \tau_2^{-1})(s + \tau_1^{-1}) + \dfrac{\mu_1 s}{\eta_2}} \tag{5}$$

Noteworthy properties of $\mu(s)$ are that in the limit $\eta_2 \longrightarrow \infty$, the material behaves as a Maxwell viscoelastic solid. In the limit $\eta_1 \longrightarrow \infty$, the material behaves as a standard linear solid with transformed shear modulus

$$\mu(s) = \frac{\mu_1 s + \mu' \tau^{-1}}{s + \tau^{-1}} \tag{6}$$

$$\mu' = \frac{\mu_1 \mu_2}{\mu_1 + \mu_2} \tag{7}$$

$$\tau = \frac{\eta_2}{\mu_1 + \mu_2} \tag{8}$$

The quantity μ' is the effective shear modulus of the material in the limit of complete relaxation, i.e., the material does not relax to a state of zero stress but retains a finite strength at large times. Since η_1 is not arbitrarily large, equation (5) demands that at sufficiently large time the material will completely relax to a state of zero stress, but if $\eta_1 \gg \eta_2$, then at times that are large compared with τ_2 but smaller than τ_1, the material will relax to a finite strength μ'.

We shall consider four physical models of postseismic deformation (Figure 4). Three of these are viscoelastic models, and the fourth is an afterslip model. In section 4.1 we focus on the model characterized by a transient rheology in the upper mantle and a Maxwell rheology in the lower crust (Figure 4a), comparing its performance with that of a univiscous rheology (Figure 4b). The remaining viscoelastic model specifies a transient rheology in the lower crust (Figure 4c) and is discussed in section 4.2. The afterslip model (Figure 4d) will be discussed in section 5.

4 Determination of rheology parameters

4.1 Biviscous mantle model

The viscoelastic relaxation component $\mathbf{v}_{\text{def}}(\hat{\mathbf{r}},t)$ is calculated according to the method of [37]. This method yields the postseismic deformation at arbitrary points and times on a spherically stratified viscoelastic medium for given dislocation sources.

One advantage of the method is that it is designed to accommodate a linear rheology directly in terms of the Laplace-transformed shear modulus, and as such the shear modulus prescribed by equation (5) may be directly implemented.

Equation (4) provides a measure of model misfit with respect to the time series observations. Although this measure allows identification of best-performing models, it does not illuminate the sensitivity of specific portions of the time series to the various model parameters. For model evaluation we therefore prefer the alternative of comparing modeled and observed velocities in specific time intervals (t_1,t_2). Model velocity at site i is

$$\mathbf{v}(\hat{\mathbf{r}}_i;t_1,t_2)=\frac{\mathbf{u}(\hat{\mathbf{r}}_i,t_2)-\mathbf{u}(\hat{\mathbf{r}}_i,t_1)}{t_2-t_1} \tag{9}$$

For each of the three Cartesian indices k=1,2,3 observed velocity $\hat{\mathbf{x}}_k(\hat{\mathbf{r}}_i)\cdot\mathbf{v}_{\rm obs}(\hat{\mathbf{r}}_i;t_1,t_2)$ with corresponding standard deviation $\sigma_{ik}(t_1,t_2)$ is derived from the observed time series by determining the best-fitting straight line fit to the $\hat{\mathbf{x}}_k(\hat{\mathbf{r}}_i)\cdot\mathbf{u}_{\rm obs}(\hat{\mathbf{r}}_i,t)$ within (t_1,t_2) and propagation of the data errors. Our measure then becomes the time-dependent velocity misfit functions

$$\chi^2{}_k(t_1,t_2)=\sum_i\frac{\left[\hat{\mathbf{x}}_k(\hat{\mathbf{r}}_i)\cdot\mathbf{v}(\hat{\mathbf{r}}_i;t_1,t_2)-\hat{\mathbf{x}}_k(\hat{\mathbf{r}}_i)\cdot\mathbf{v}_{\rm obs}(\hat{\mathbf{r}}_i;t_1,t_2)\right]^2}{\left[\sigma_{ik}(t_1,t_2)\right]^2} \tag{10}$$

The summation over i is over the combined SCIGN and USGS data sets.

Figure 5a summarizes the rheologies chosen for the upper crust (purely elastic), lower crust (Maxwell viscoelastic), and upper mantle (Burghers body). Among the five parameters that control the complete rheology, only the steady state shear and bulk moduli $\{\mu_1, \kappa_1\}$ are known with reasonable certainty. Noting equation (7), we consider two values of μ': $\mu' = 0.5 \times \mu_1$ (50% relaxation during transient phase) and $\mu' = 0.75 \times \mu_1$ (25% relaxation during transient phase). It is necessary to choose a relevant range of γ, defined as the ratio of steady state viscosity between the crust and mantle. Although previous work [15] suggests a large ratio in effective viscosity, this is not directly related to steady state viscosity. We consider three possible values for this ratio: γ=1, 7, and 20. The remaining unknown parameters are then η_2 and η_1 -- the transient and steady state viscosities of the mantle.

We perform a grid search for η_2 and η_1 based on fitting all 135 time series with

a model of postseismic relaxation and evaluating misfit with equation (10) for each model using three time intervals (t_1,t_2)=(10 days , 3 months), (10 days , 9 months), and (3 months , 2.5 years). The results are shown in Figure 6. Among the values of γ considered, only values $\gamma \geq 7$ provide a satisfactory fit to the vertical velocity field during the later time period. Although only slightly better fits to the complete dataset are achieved with γ=7 compared with γ=20, for concreteness we choose the value γ=7 for further consideration. Examining Figure 6c,d, between the two values of μ' considered, the fits over the later (3 months to 2.5 year) time period are similar, but over the earlier time periods the smaller value $\mu'=0.5\times\mu_1$ provides a vastly better fit to the data. In this case (Figure 6c), the misfit patterns for the later time period have minimum misfit at roughly constant η_1 with little sensitivity to η_2. In contrast, the minimum misfit domain for the early time period defines roughly a line of slope −1 in $\log\eta_2/\eta_1 - \log\eta_1$ space, or simply $\eta_2 \sim$ constant. The intersection of these two domains yields a model prescribed by values $\mu'=0.5\times\mu_1$ (equivalent to $\mu_2 = \mu_1$, i.e., a Jeffreys solid), γ=7, $\eta_1 = 4.6\times10^{18}$ Pa s, and $\eta_2 = 0.35\times\eta_1 = 1.6\times10^{17}$ Pa s. This model is henceforth considered the preferred model in the remainder of this paper. The velocity and displacement fields derived from this model are consistent with essentially all data sets considered, but we note that only slightly worse fits are obtained by a model with similar μ' and η_1 but somewhat higher transient viscosity $\eta_2 \sim 0.1\times\eta_1 \sim 5\times10^{17}$ Pa s. However, η_2 less than about 10^{17} Pa s or greater than about 5×10^{17} Pa s is inconsistent with the observations.

We compare the performance of the preferred biviscous model with the equivalent univiscous model ($\eta_2=\infty$, i.e., Maxwell viscoelastic), other factors being equal. A grid search for η_1 yields minimum misfit at $\eta_1=4.6\times10^{18}$ Pa s. Table 1 lists the misfit values of the best biviscous and univiscous models and the number of time series with useful velocity estimates. Application of an F-test [38] to the early-period horizontal data alone shows that the biviscous model (variable μ', η_1, η_2) is a significant improvement to the univiscous model (variable η_1) at the 99.0% confidence level. The principal shortcoming of the univiscous model is that, since its material relaxation time is ~2 years, it generally does not capture the amplitude of the transient observed during the first 0.2 year (Figure 3c,d). This is verified by comparison of observed and calculated horizontal velocities within the two considered time periods

(Figure 7). It shows that the biviscous model adequately accounts for the observed velocities at both early and later time periods. The univiscous model exhibits similarly good agreement during the later time period but systematic disagreement during the early time period when modeled velocities are generally smaller than observed.

4.2 Biviscous lower crust model

The biviscous lower crust model is shown schematically in Figure 4c and parameterized in Figure 5b. We find that there is no model in this class which fits the horizontal and vertical data simultaneously. Illustrative examples are shown in Figure 9 for various slices of model space. Each misfit curve has been scaled by the misfit achieved by the preferred biviscous mantle model. For the slice shown in Figure 9a (γ=7, μ'=0.5×μ_1, and η_2 / η_1 = 0.004), three of the curves approach unity and thus fit the corresponding data set equally well as the biviscous mantle model, but the fourth and fifth, corresponding to uplift during the early postseismic time period (10 days to 3 months, 10 days to 9 months), do not. The model obtained where the three satisfactory curves approximately intersect has lower crust viscosities of $\eta_1 \sim 1.9\times10^{19}$ Pa s and $\eta_2 \sim 7.5\times10^{16}$ Pa s, and mantle viscosity $\eta_m \sim 2.7\times10^{18}$ Pa s. The predictions of the uplift pattern for this model are shown in Figure 8b where they may be compared with the predictions of the preferred biviscous mantle model (Figure 8a). The patterns of calculated vertical response in the 3 month to 2.5 year period are similar for both the biviscous lower crust and biviscous mantle models, but the models diverge as the time period encompasses more of the earlier postseismic epoch, with the biviscous lower crust model performing progressively worse. Among other models in this class, increasing the ratio η_2/η_1 (Figure 9c,d) worsens the horizontal-vertical incompatibility; decreasing the ratio further produces behavior indistinguishable from the univiscous model. As was found for the class of biviscous mantle models, taking smaller γ (Figure 9b,d) does not improve the fit of the vertical data for the early periods and clearly worsens the fit of the vertical data for the later time period.

5 Discussion

The fits of the selected time series using the preferred biviscous mantle model are shown with the red solid curves in Figure 3. The model fits the primary patterns

exhibited by this data: early, rapid transient behavior for the first ~0.2 years followed by deformation at slower rates for the succeeding 2.3 years. Most time series are well fit for both the early and late periods as well as the transition between transient and steady state relaxation. This is also demonstrated by the overall agreement between predicted and observed horizontal velocity components (Figure 7a)

The vertical GPS time series are also fit fairly well, as shown in Figure 8a for three different time periods, considering the errors generally present in vertical GPS measurements. The predicted spatial uplift pattern is shown in Figure 10 where it is compared with compiled SCIGN uplift measurements for three postseismic epochs. The observed vertical velocity pattern is consistent with the predicted quadrant pattern for all time periods and further shows that the sign of the quadrant pattern is maintained with time. The class of biviscous lower crust models generally predicts a reversal in the sign of the quadrant pattern as time progresses (Figure 8b), and the lack of such a reversal in the observations is the principal shortcoming of that model class. We note that the observed GPS uplift pattern is very similar to that revealed by InSAR for the first 9 months postseismic period [15], showing that vertical GPS and InSAR data carry similar implications for the rheology of this region.

An alternative postseismic deformation model would involve afterslip on discrete slip surfaces beneath those which ruptured in the Hector Mine earthquake (Figure 4d). We construct an afterslip model consisting of the downdip extensions (from 36 - 16 km depth) of representative coseismic rupture planes (the same geometry as in [15]) with a specified right-lateral slip within three different time intervals (1 meter slip from 10 days to 3 months; 2 meters slip from 10 days to 9 months; 1 meter slip from 3 months to 2.5 years). The slip is chosen to yield approximate agreement with the observed horizontal velocity field, but our concern here is the vertical velocity field. The resulting postseismic uplift pattern (Figure 8c) is anticorrelated with the observed postseismic uplift pattern for all time periods. Most of the sites are simply located in the wrong uplift quadrant, and a change in afterslip parameters is unlikely to remedy this situation, assuming that its slip must be in the right-lateral sense. In addition, the early-period (10 days to 3 months) horizontal velocity field generally exhibits large far-field postseismic velocity. For example, the East-velocity of BSRY and WOMT, both of which are >~60 km from the coseismic rupture, are large (Figure 7a). In order to fit these data simultaneously with smaller postseismic velocities of more nearby

sites would require afterslip planes penetrating well into the mantle, which seems implausible.

For a strike-slip faulting event, poroelastic rebound of the upper crust, driven by dissipation of fluid pressure gradients created by the coseismic stress field, produces a postseismic uplift pattern opposite to the coseismic uplift pattern. This is qualitatively similar to that pattern predicted by the preferred biviscous mantle model, and significant poroelastic effects have been documented for the first ~5 weeks following both the 1992 Landers earthquake [17] and June 17, 2000 SISZ Iceland earthquake [39]. However, the spatial scale of demonstrated poroelastic effects is ~3 km, in accord with physical considerations based on the expected sharp decrease in permeability below 2–3 km depth [40]. This contrasts with the >~ 20 km scale of postseismic uplift following the Hector Mine earthquake as displayed in Figure 10. (The two most rapidly uplifting sites during the early postseismic periods are BSRY and LDES, both >30 km from the locus of coseismic slip.) Although the precise properties of poroelastic flow should be confirmed with realistic modeling, it is likely that its long wavelength signal in our data set is very small, especially with the exclusion of the first 10 days postseismic observations.

Our results suggest that the upper mantle beneath the Mojave Desert exhibits a transient rheology with two material decay constants of $\tau_2 \sim 0.07$ and $\tau_1 \sim 2$ years. If true, it raises the question of the mechanisms of relaxation responsible for the two very different relaxation regimes. Creep experiments on mineral samples at constant applied stress typically yield a transient phase of rapid strain rate followed by a phase of slower but essentially constant strain rate [20]. The later phase is associated with steady state creep, for which many mechanisms are available [41–43]. In general, it is thought that the relative resistance to dislocation glide versus dislocation climb [21] controls the nature of the transient stage. However, Karato [44] points out that "no systematic studies of transient creep have been made on olivine and olivine rich rocks."

From the bound $\gamma \geq \sim 7$ and the estimate of steady state lower crust viscosity of $\sim 3.2 \times 10^{19}$ Pa s, a relatively strong crust appears necessary to explain the Hector Mine postseismic GPS data. For comparison, an effective lower crust viscosity $\sim 10^{20}$ Pa s has been inferred for the Lake Mead, Nevada region [45] and for the epicentral region

of the 1959 Hebgen Lake earthquake [46].

The Kelvin element associated with transient viscosity $\eta_2 = 1.6\times10^{17}$ Pa s inferred here is presumably one of several relaxation elements that compose an absorption band model of seismic wave attenuation. With $\eta_1 \gg \eta_2$, this value of η_2 is comparable with the average-Earth value $\eta_2 \sim O(10^{16})$ Pa s estimated to fit seismic Q of Earth's lowest free oscillations with a single standard linear solid rheology [22]. The present modeling leaves open the question of whether the larger viscosity $\eta_1 \sim 5\times10^{18}$ Pa s is the true long term viscosity of the upper mantle beneath the Mojave Desert, or whether it is itself another component of a generalized Burghers body rheology with a long term viscosity closer to $\sim10^{21}$ Pa s as suggested by mantle convection studies. This question is worth pursuing since it carries implications for the transition from anelastic to viscous behavior in Earth's upper mantle. Karato [44] cites experimental evidence that the transient stage persists until a net strain of 1-2% is attained, which is thought to require 1000s of years in postglacial rebound studies. If η_1 is indeed the long term viscosity then it would imply that, on a local scale, the transition can take place at a much shorter time scale than on the continental-wide scale. It would also imply that the transition from anelastic to viscous deformation mechanisms has taken place within the time frame of the Hector Mine postseismic epoch. With a mantle strain rate of about 10^{-5}/yr during the early post-Hector Mine period, clearly very little strain would accumulate in just a few weeks. I suggest that the bulk deformation behavior in the uppermost mantle may differ from the microscopic deformation behavior, possibly because of the presence of a sub-Moho macroscopic rock fabric of the type recently proposed by Fuchs et al. [47]. In any case, the present results appear to confirm Yuen and Peltier's assertion [22] that the quasi-static deformation is partially "supported by the anelastic component of the complete rheology."

6 Conclusions

The principal results of this study are: (1) Three-dimensional surface deformation measured by GPS in the epicentral region of the 1999 Hector Mine earthquake for the first 2.5 years after the earthquake are explained with a model of transient mantle rheology, specifically a linear biviscous rheology. (2) A grid search performed on the three-component GPS time series for both the steady state mantle viscosity η_1 and

transient viscosity η_2 yield values of $\eta_1 \sim 4.6\times10^{18}$ Pa s and $\eta_2 = 1.6\times10^{17}$ Pa s. A Jeffreys solid (equal transient and steady state shear moduli) appears most consistent with the observations. (3) This model explains the observed pattern of rapid deformation during the first 0.2 year followed by an indefinite (and likely continuing) period of slower deformation, as well as the pattern of time-dependent postseismic uplift. (4) Alternative models considered such as a transient rheology localized in the lower crust, a linear univiscous rheology, or deep afterslip fail to explain one or more of the essential features of the observations.

The plausibility of the transient rheology model does not rule out other possibilities to explain the postseismic deformation patterns. Another chief candidate mechanism is nonlinear (stress and temperature-dependent) rheology of the lower crust and upper mantle [15]. This appears capable of explaining at least the horizontal postseismic GPS observations (Andy Freed, personal communication). All models considered up to the present are likely oversimplifications of the true rheology, which is likely laterally variable and characterized by several anelastic deformation mechanisms at all times. Regardless of the precise mechanisms, it appears that postseismic flow deep beneath the coseismic rupture and the involvement of processes occurring over several time scales, are robust properties of the postseismic epoch.

Acknowledgements. I am grateful to Jim Savage for instructive discussions which stimulated this work. I thank him, Steve Kirby, Marleen Nyst, and Wayne Thatcher for their valuable internal reviews of this paper and Ken Hudnut for advice concerning SCIGN data processing. This paper has benefitted from discussions with Roland Bürgmann, Louise Kellogg, and Don Turcotte and the constructive comments of Scott King, Russ Pysklywec, and two anonymous reviewers.

References

[1] S. King, Models of mantle viscosity, in: T.J. Ahrens (Ed.), *Mineral Physics and Crystallography: A Handbook of Physical Constants, AGU Reference Shelf 2*, American Geophysical Union, Washington, DC, 1995, pp. 227-236.

[2] B.H. Hager, R.J. O'Connell, A simple global model of plate dynamics and mantle convection, *J. Geophys. Res. 86* (1981) 4843-4867.

[3] Y. Ricard, C. Vigny, Mantle dynamics with induced plate tectonics, *J. Geophys. Res. 94* (1989) 17,543-17,559.

[4] M.K. Clark, L.H. Royden, Topographic ooze: Building the eastern margin of Tibet by lower crustal flow, *Geology 28* (2000) 703-706.

[5] B.H. Hager, Mantle viscosity: A comparison of models from postglacial rebound and from the geoid, plate driving forces, and advected heat flux, in: R. Sabadini, K. Lambeck, and E. Boschi (Eds.), *Glacial Isostacy, Sea Level and Mantle Rheology*, Kluwer Academic Publishers, London, 1991, pp. 493-513.

[6] A. Nur, G. Mavko, Postseismic viscoelastic rebound, *Science 183* (1974) 204-206.

[7] W. Thatcher, T. Matsuda, T. Kato, J.B. Rundle, Lithospheric loading by the 1896 Riku–u earthquake, northern Japan: Implications for plate flexure and asthenospheric rheology, *J. Geophys. Res. 85* (1980) 6429-6435.

[8] S.C. Cohen, A multilayer model of time dependent deformation following an earthquake on a strike slip fault, *J. Geophys. Res. 87* (1982) 5409-5421.

[9] J.B. Rundle, Viscoelastic-gravitational deformation by a rectangular thrust fault in a layered Earth, *J. Geophys. Res. 87* (1982) 7787-7796.

[10] W. Thatcher, Nonlinear strain buildup and the earthquake cycle on the San Andreas fault, *J. Geophys. Res. 88* (1983) 5893-5902.

[11] K. Miyashita, A model of plate convergence in southwest Japan, inferred from leveling data associated with the 1946 Nankaido earthquake, *J. Phys. Earth 35* (1987) 449-467.

[12] T. Tabei, Crustal movements in the inner zone of southwest Japan associated with stress relaxation after major earthquakes, *J. Phys. Earth 37* (1989) 101-131.

[13] P.A. Rydelek, I.S. Sacks, Asthenospheric viscosity and stress diffusion: A mechanism to explain correlated earthquakes and surface deformations in

northeast Japan, *Geophys. J. Int. 100* (1990) 39-58.

[14] F.F. Pollitz, I.S. Sacks, Modeling of postseismic relaxation following the Great 1857 earthquake, southern California, *Bull. Seismol. Soc. Am. 82* (1992) 454-480.

[15] F.F. Pollitz, C. Wicks, W. Thatcher, Mantle flow beneath a continental strike-slip fault: Postseismic deformation after the 1999 Hector Mine earthquake, *Science 293* (2001) 1814-1818.

[16] Z.-K. Shen et al., Postseismic deformation following the Landers earthquake, California, 28 June 1992, *Bull. Seismol. Soc. Am. 84* (1994) 780-791.

[17] G. Peltzer, P. Rosen, F. Rogez, K. Hudnut, Poro-elastic rebound along the Landers 1992 earthquake surface rupture, *J. Geophys. Res. 103* (1998) 30,131-30,145.

[18] J. Deng, M. Gurnis, H. Kanamori, E. Hauksson, Viscoelastic flow in the lower crust after the 1992 Landers, California, earthquake, *Science 282* (1998) 1689-1692.

[19] F.F. Pollitz, G. Peltzer, R. Bürgmann, Mobility of continental mantle: Evidence from postseismic geodetic observations following the 1992 Landers earthquake, *J. Geophys. Res. 105* (2000) 8035-8054.

[20] N.L. Carter, S. Kirby, Transient creep and semi-brittle behavior of crystalline rocks, *Pure Appl. Geophys. 116* (1978) 807-839.

[21] J.B. Minster, D.L. Anderson, A model of dislocation-controlled rheology for the mantle, *Philos. Trans. R. Soc. London 299* (1981) 319-356.

[22] D.A. Yuen, W.R. Peltier, Normal modes of the viscoelastic earth, *Geophys. J. Roy. Astr. Soc., 69* (1982) 495-526.

[23] E.R. Ivins, Transient creep of a composite lower crust, 2, A polymineralic basis for rapidly evolving postseismic deformation modes, *J. Geophys. Res. 101* (1996) 28,005-28,028.

[24] H.J. Melosh, Rheology of the Earth: Theory and Observation, in: A.M. Dziewonski and E. Boschi (Eds.), *Physics of the Earth's Interior, Proceedings of the 1979 Enrico fermi Summer School, Varenna, Italy,* North Holland, Amsterdam, 1980, pp. 318-336.

[25] W.R. Peltier, P. Wu, D. Yuen, The viscosities of the Earth's mantle, in: F.D. Stacey, A. Nicolas, M.S. Peterson (Eds.), *Anelasticity in the Earth, American Geophysical Union Geodynamics Series*, Washington, DC, 1981, pp. 59-71.

[26] E. Hauksson, L.M. Jones, K. Hutton, D. Eberhart-Phillips, The 1992 Landers earthquake sequence: Seismological observations, *J. Geophys. Res. 98* (1993) 19,835-19,858.

[27] http://pasadena.wr.usgs.gov/scign/cgi-bin/datafile.cgi

[28] http://quake.wr.usgs.gov/research/deformation/gps/auto/HectorMine

[29] K.W. Hudnut et al., Continuous GPS observationsof postseismic deformation following the 16 October 1999 Hector Mine earthquake (M_w 7.1), *Bull. Seismol. Soc. Am. 92* (2002) 1403-1422.

[30] J.C. Savage, J.L. Svarc, W.H. Prescott, Strain accumulation near Yucca Mountain, 1993-1998, *J. Geophys. Res. 106* (2001) 16,483-16,488.

[31]. G. Blewitt, D. Lavallee, Effect of annual signals on geodetic velocity, *J. Geophys. Res., 107* (2002) ETG 9, 1-11.

[32] J.C. Savage, J.L. Svarc, Postseismic deformation associated with the 1992 M_w = 7.3 Landers earthquake, southern California, *J. Geophys. Res. 102* (1997) 7565-7577.

[33] D.J. Wald, D.J., T. H. Heaton, Spatial and temporal distribution of slip for the 1992 Landers, California, earthquake, *Bull. Seismol. Soc. Am. 84* (1994) 668-691.

[34] D.S. Dreger, A. Kaverina, Seismic remote sensing for the earthquake source process and near-source strong shaking: a case study of the October 16, 1999 Hector Mine earthquake, *Geophys. Res. Lett. 27* (2000) 1941-1944.

[35] K.B. Richards-Dinger, P.M. Shearer, Earthquake locations in southern California obtained using source-specific station terms, *J. Geophys. Res. 105* (2000) 10,939-10,960.

[36] J. Qu, T.L. Teng, J. Wang, Modeling of short-period surface-wave propagation in southern California, *Bull. Seismol. Soc. Am. 84* (1994) 596-612.

[37] F.F. Pollitz, Gravitational-viscoelastic postseismic relaxation on a layered spherical Earth, *J. Geophys., Res. 102* (1997) 17,921-17,941.

[38] S. Stein, R. Gordon, Statistical tests of additional plate boundaries from plate motion inversions, *Earth Planet. Sci. Lett. 69* (1984) 400-412.

[39] S. Jonsson, R. Pedersen, P. Segall, G. Björnsson, Postseismic poro-elastic deformation in south Iceland observed with radar interferometry: Implications for aftershock decay, *EOS, Trans. Am. Geophys. Un., 83(47)* (2002) F364.

[40] S.E. Ingebritsen, C.E. Manning, Geological implications of a permeability-depth

curve for the continental crust, *Geology, 27* (1999) 1107-1110.

[41] G. Ranalli, Rheology of the Earth: Deformation and Flow Processes in Geophysics and Geodynamics, Allen and Unwin, Boston, 1987, 366 pp.

[42] S.-I. Karato, P. Wu, Rheology of the upper mantle: A synthesis, *Science 260* (1993) 771-778.

[43] G. Hirth, D.L. Kohlstedt, Water in the oceanic upper mantle: implications for rheology, melt extraction, and the evolution of the lithosphere, *Earth Planet. Sci. Lett. 144* (1996) 93-108.

[44] S.-I. Karato, Defects and plastic deformation in olivine, in: S.-I. Karato, M. Toriumi (Eds.), *Rheology of Solids and of the Earth*, Oxford University Press, Oxford, 1989.

[45] G. Kaufmann, F. Amelung, Reservoir-induced deformation and continental rheology in vicinity of Lake Mead, Nevada, *J. Geophys. Res. 105* (2000) 16,341-16,358.

[46] T. Nishimura, W. Thatcher, Rheology of the lithosphere inferred from postseismic uplift following the 1959 Hebgen Lake earthquake, *J. Geophys. Res.*, submitted (2002).

[47] K. Fuchs, M. Tittgemeyer, T. Ryberg, F. Wenzel, W. Mooney, Global significance of a sub-Moho boundary layer (SMBL) deduced from high-resolution seismic observations,*International Geology Review, 44* (2002) 671 - 685.

Figure Captions

Figure 1. A Burghers body rheology consists of a Maxwell element in series with Kelvin element, or equivalently a dashpot in series with a Zener standard linear solid. The quantities η_1 and $\{\mu_1, \kappa_1\}$ are the steady state viscosity and {shear, bulk} modulus, respectively, and η_2 and μ_2 are the transient viscosity and shear modulus, respectively.

Figure 2. Locations of 29 GPS sites used in this study. Sixteen of them are part of the SCIGN continuous GPS network; 13 are USGS campaign GPS sites. Red and orange lines denote surface traces of the 1999 Hector Mine and 1992 Landers earthquakes, respectively.

Figure 3 (a) Three-component GPS time series for the first 2.5 years following the Hector Mine earthquake at three selected sites as recorded by the SCIGN continuous stations. Red curves are the predicted displacements (e.g., $\mathbf{u}(\hat{\mathbf{r}}_i, t)$ as prescribed by equation (3)) based on the preferred transient rheology model (explained in section 4). Dashed green curves are the predicted displacements on a transient lower crust rheology model (section 5). Dashed blue curves are the predicted displacements on a univiscous rheology model (section 4). (b) GPS time series at three selected sites as recorded by the USGS campaign measurements, with standard errors. (c) and (d) are a close-up view of the same time series shown in (a) and (b) for the first 0.25 years.

Figure 4. Four different candidate models for postseismic deformation considered in this study. (a), (b), and (c) are viscoelastic models with various combinations of Burghers body and Maxwell rheologies in the lower crust and upper mantle. Case (b) is referred to as "univiscous rheology" in the text. The afterslip model in (d) is shown schematically as discontinuous slip in the deeper extension of the coseismic slip region.

Figure 5. (a) Parameterization of a biviscous upper mantle model. Each of the upper crust, lower crust, and upper mantle is taken to have uniform material properties. The ratio of crust-to-mantle viscosity is denoted by γ. The lower crust and upper mantle are assumed to behave as a Maxwell viscoelastic solid and

Burghers body, respectively. Five parameters are needed to describe the mantle rheology. The steady state shear and bulk moduli μ_1 and κ_1 are given in (c). The transient shear modulus μ_2 is constrained by the choice of μ', which prescribes μ_2 through equation (7). The remaining parameters η_1 (steady state viscosity) and η_2 (transient viscosity) are variable. (b) Parameterization of a biviscous lower crust model. The lower crust and upper mantle are assumed to behave as a Burghers body and Maxwell viscoelastic solid, respectively. The ratio of crust-to-mantle viscosity is denoted by γ. (c) Shear modulus μ_1 and bulk modulus as a function of depth as constrained by seismic information [36].

Figure 6. Misfit $\chi^2_k(t_1,t_2)$ of model velocity with respect to observed observed velocity as a function of η_1 and the ratio η_2/η_1 for (a, c, e) $\mu' = 0.5\times\mu_1$ and (b, d, f) $\mu' = 0.75\times\mu_1$. Parts (a, b), (c, d), and (e, f) correspond to γ=1, 7, and 20, respectively. Referring to equation (10), horizontal misfit is the sum $\chi^2_1 + \chi^2_2$, and vertical misfit is χ^2_3. Note that the minimum misfit domains obtained for the early (10 days to 3 months; 10 days to 9 months) and later (3 months to 2.5 years) time periods are compatible in (c) but incompatible in (d). Preferred biviscous model (section 4) is indicated with filled black circle in the subplots of (c).

Figure 7. Predicted horizontal velocities from (a) biviscous upper mantle rheology model (preferred model of Figure 6c) and (b) univiscous (lower crust + upper mantle) model are compared with horizontal velocities derived from SCIGN continuous and USGS campaign time series for two postseismic time periods. Error bars represent one standard deviation about the plotted point. Only those velocity estimates with standard deviation less than 30 mm/yr are shown. In each plot, the best-fitting line constrained to pass through the origin is indicated together with the value of its slope and standard deviation. A slope of 1 would correspond to perfect agreement between model and observation. The slope much greater than 1 for the univiscous model during the 10 days - 3 months period indicates model velocities that tend to underpredict observed velocities during the early postseismic period.

Figure 8. Predicted uplift rates from (a) biviscous upper mantle rheology model

(preferred model of Figure 6c), (b) biviscous lower crust model defined in the text, and (c) afterslip model are compared with uplift rates derived from SCIGN continuous time series for three postseismic time periods. Error bars represent one standard deviation about the plotted point. Only those velocity estimates with standard deviation less than 30 mm/yr are shown. In each plot, the best-fitting line constrained to pass through the origin is indicated together with the value of its slope and standard deviation. A slope of 1 would correspond to perfect agreement between model and observation.

Figure 9. Misfit of various velocity fields as a function of η_1 for various slices of the biviscous lower crust model. Referring to equation (10), horizontal misfit is the sum $\chi^2_1 + \chi^2_2$, and vertical misfit is χ^2_3. All models have fixed $\mu' = 0.5 \times \mu_1$. For each case, the misfit has been divided by the corresponding misfit achieved by the preferred biviscous mantle model. A value of unity thus corresponds to identical fit of a dataset by the two models.

Figure 10. Uplift of SCIGN sites with useful measurements (standard deviation less than 30 mm/yr) during three postseismic periods, shown with continous vertical bars (positive uplift) or dashed bars (negative uplift). These are compared with the corresponding predictions of the preferred biviscous model shown by the colored pattern. The area is as viewed from 45˚ from vertical.

Table 1

Velocity-misfit of biviscous and univiscous models

	10 days-3 months		10 days-9 months		3 month -2.5 years	
	horizontal	vertical	horizontal	vertical	horizontal	vertical
[a] χ^2_{bi}	112.6	0.48	1391	12.1	18508	145.4
[b] χ^2_{uni}	221.8	1.64	2428	15.2	18525	146.0
N	16	5	29	14	29	16

[a] χ^2_{bi} is the misfit computed on the preferred biviscous model (α=0.5 η_1, η_1=4.6$\cdot$10^{18} Pa s, η_2=1.6$\cdot$10^{17} Pa s, β=7).

[b] χ^2_{uni} is the misfit computed on the best-fitting univiscous model (η_1=4.6$\cdot$10^{18} Pa s, η_2=∞, β=7).

All misfits are computed with equation (10).

N is the number of sites with useful velocity measurements.

Figure 1

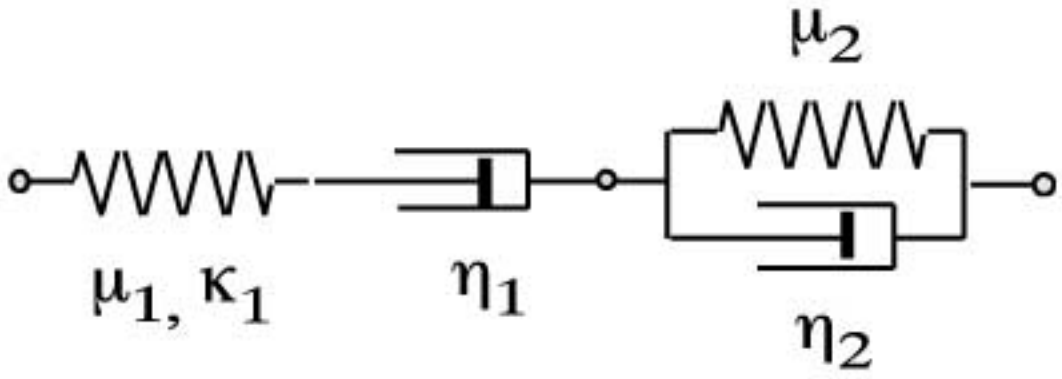

Maxwell element Kelvin element

Figure 2

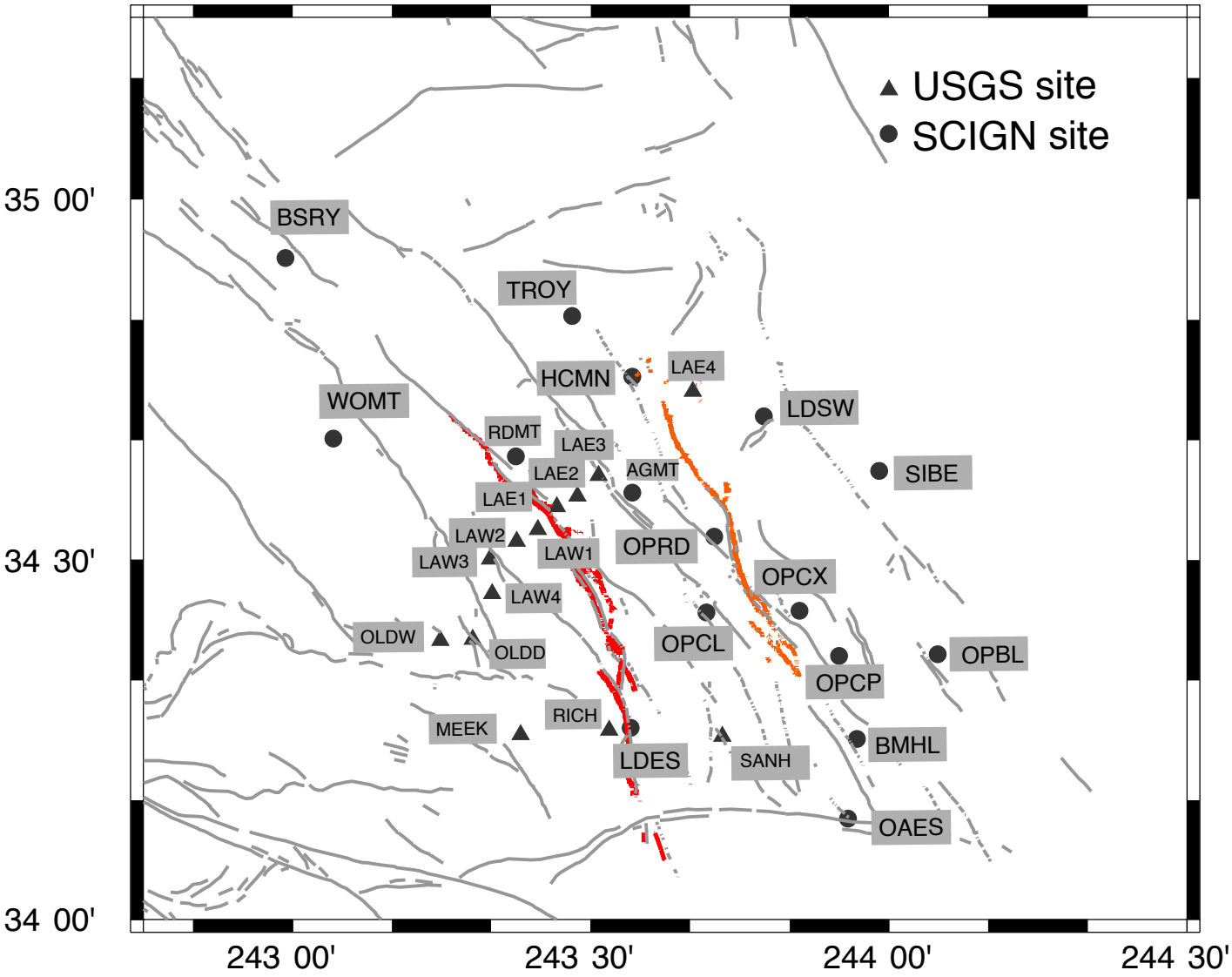
USGS site
SCIGN site
BSRY
TROY
HCMN
LAE4
WOMT
LDSW
RDMT
LAE3
LAE2
AGMT
SIBE
LAE1
LAW2
LAW1
OPRD
LAW3
OPCX
LAW4
OLDW
OLDD
OPCL
OPBL
OPCP
RICH
MEEK
BMHL
LDES
SANH
OAES
35 00'
34 30'
34 00'
243 00'
243 30'
244 00'
244 30'

Figure 3

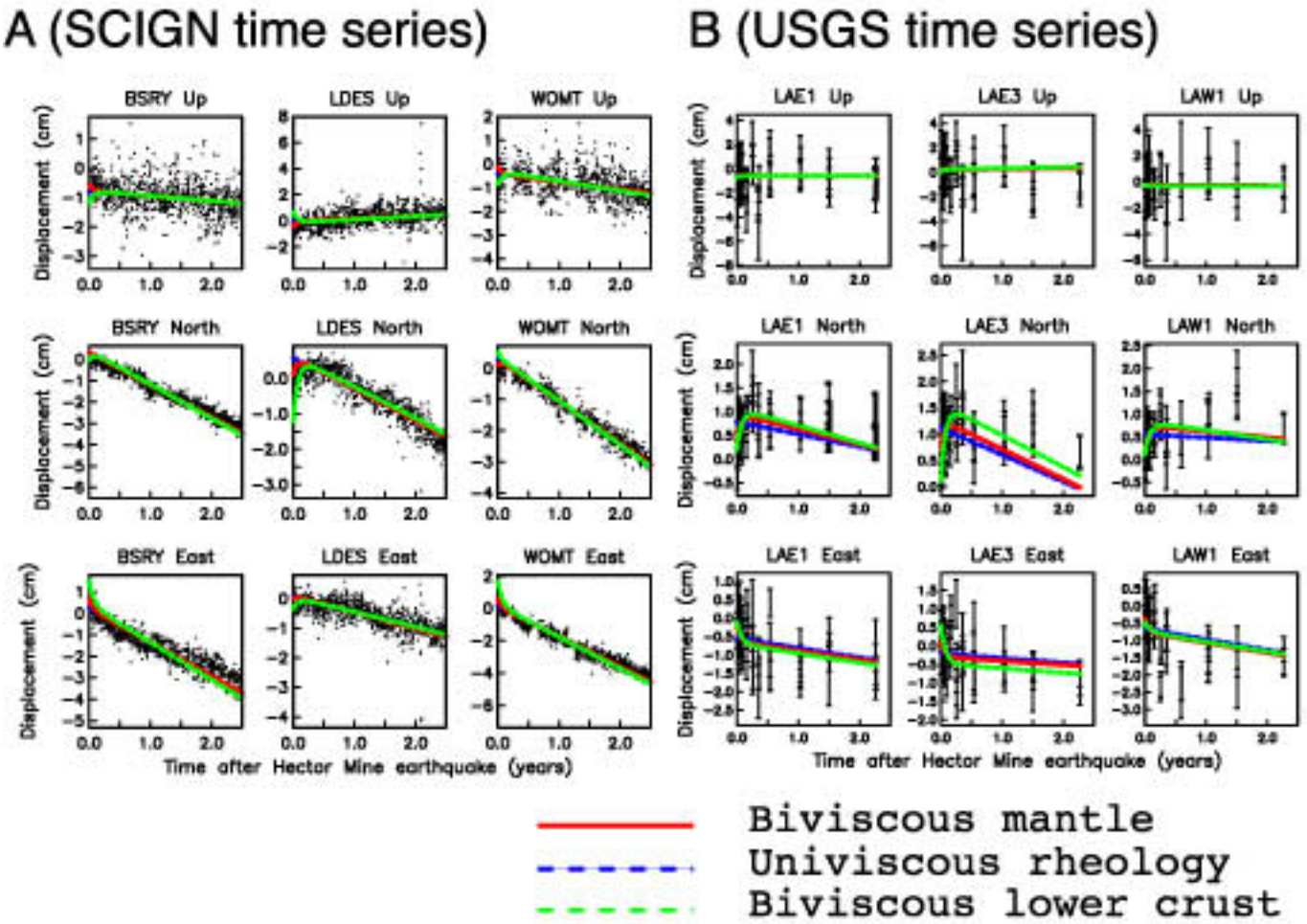
A (SCIGN time series)
B (USGS time series)
BSRY Up
LDES Up
WOMT Up
LAE1 Up
LAE3 Up
LAW1 Up
BSRY North
LDES North
WOMT North
LAE1 North
LAE3 North
LAW1 North
BSRY East
LDES East
WOMT East
LAE1 East
LAE3 East
LAW1 East
Displacement (cm)
Time after Hector Mine earthquake (years)
Biviscous mantle
Univiscous rheology
Biviscous lower crust
C (SCIGN time series)
D (USGS time series)

Figure 4

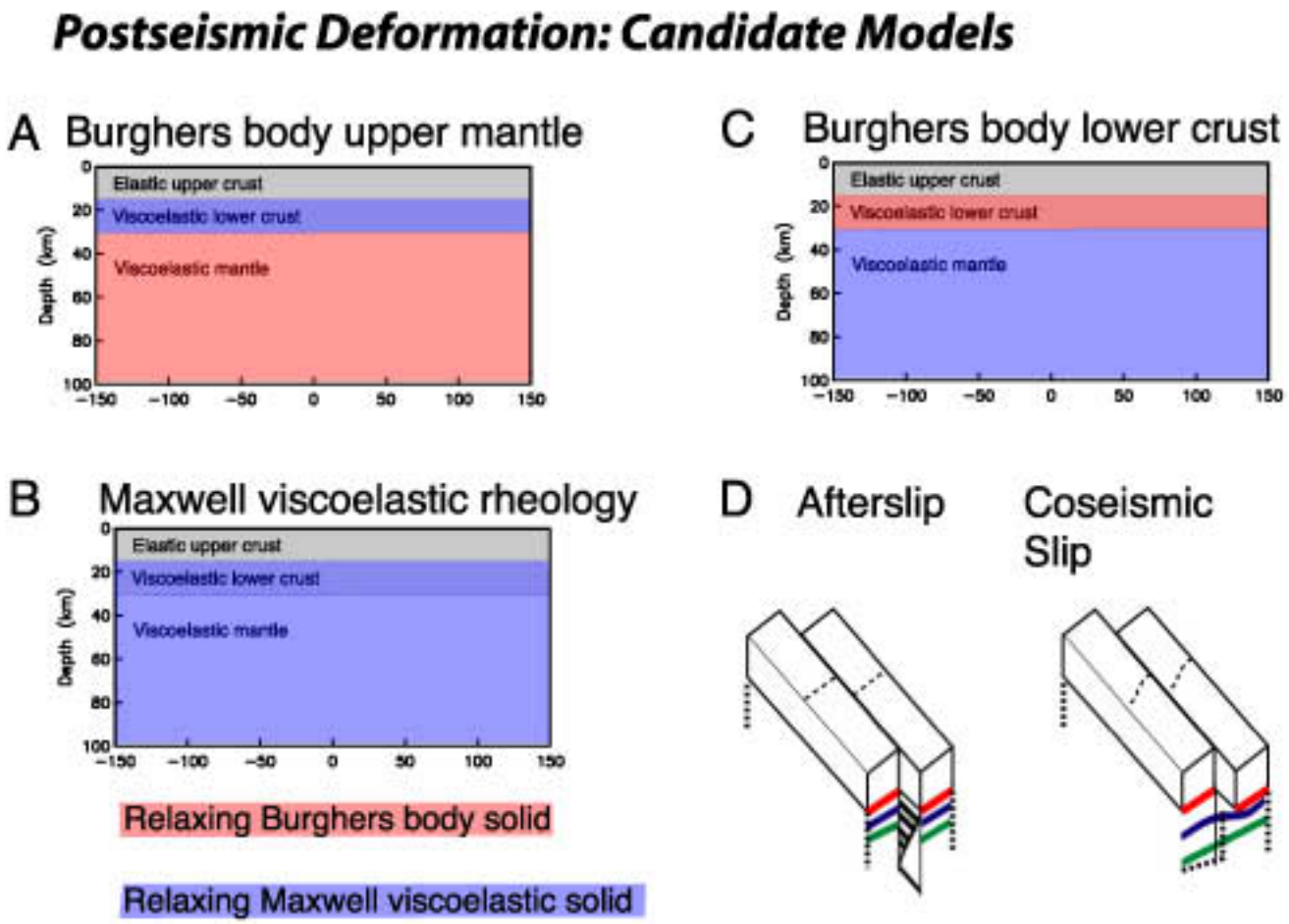
Postseismic Deformation: Candidate Models
A Burghers body upper mantle
Elastic upper crust
Viscoelastic lower crust
Viscoelastic mantle
Depth (km)
0
20
40
60
80
100
−150
−100
−50
0
50
100
150
C Burghers body lower crust
Elastic upper crust
Viscoelastic lower crust
Viscoelastic mantle
Depth (km)
B Maxwell viscoelastic rheology
Elastic upper crust
Viscoelastic lower crust
Viscoelastic mantle
Depth (km)
Relaxing Burghers body solid
Relaxing Maxwell viscoelastic solid
D Afterslip
Coseismic Slip

Figure 5

A

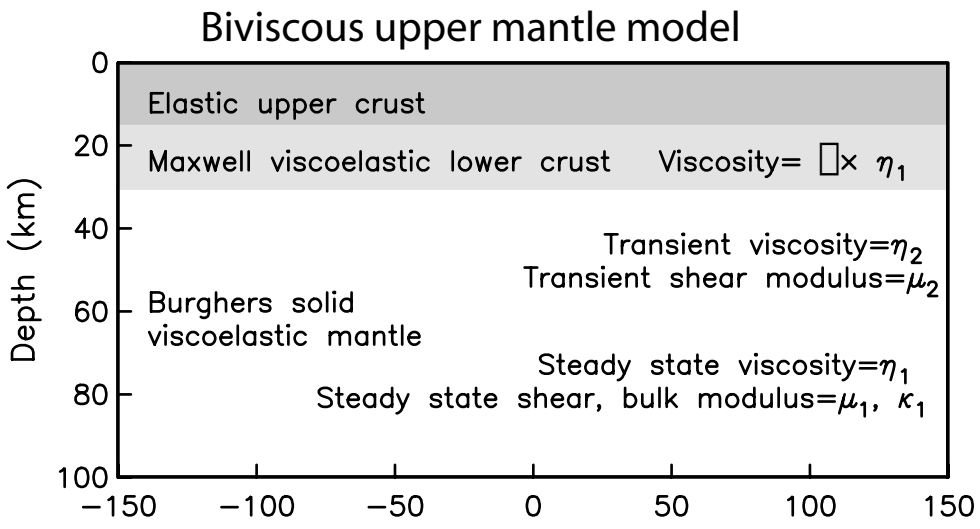
Biviscous upper mantle model
Elastic upper crust
Maxwell viscoelastic lower crust
Viscosity= □× η1
Transient viscosity=η2
Transient shear modulus=μ2
Burghers solid
viscoelastic mantle
Steady state viscosity=η1
Steady state shear, bulk modulus=μ1, κ1
Depth (km)
0
20
40
60
80
100
−150
−100
−50
0
50
100
150

B

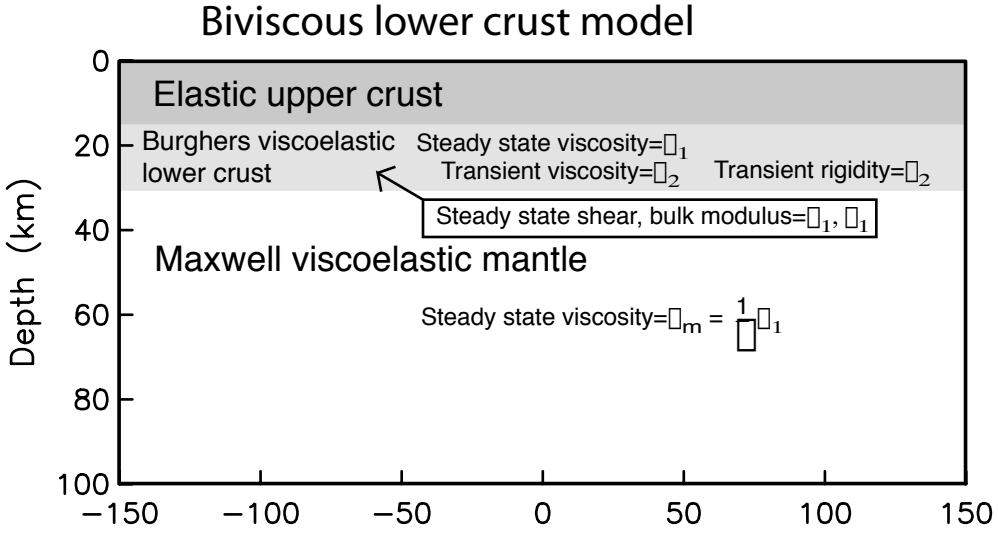
Biviscous lower crust model
Elastic upper crust
Burghers viscoelastic
lower crust
Steady state viscosity=□1
Transient viscosity=□2
Transient rigidity=□2
Steady state shear, bulk modulus=□1, □1
Maxwell viscoelastic mantle
Steady state viscosity=□m = 1/□□1
Depth (km)
0
20
40
60
80
100
−150
−100
−50
0
50
100
150

C

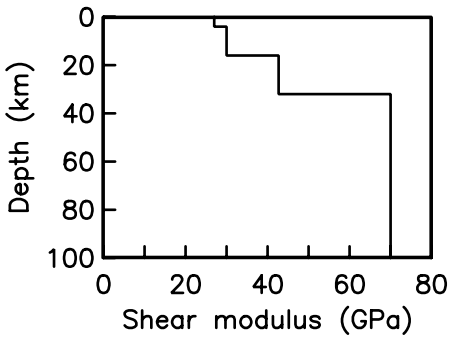
Depth (km)
0
20
40
60
80
100
0
20
40
60
80
Shear modulus (GPa)

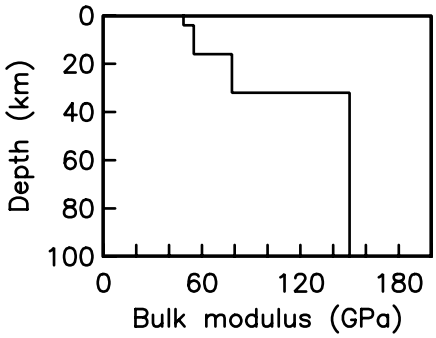
Depth (km)
0
20
40
60
80
100
0
60
120
180
Bulk modulus (GPa)

Figure 6

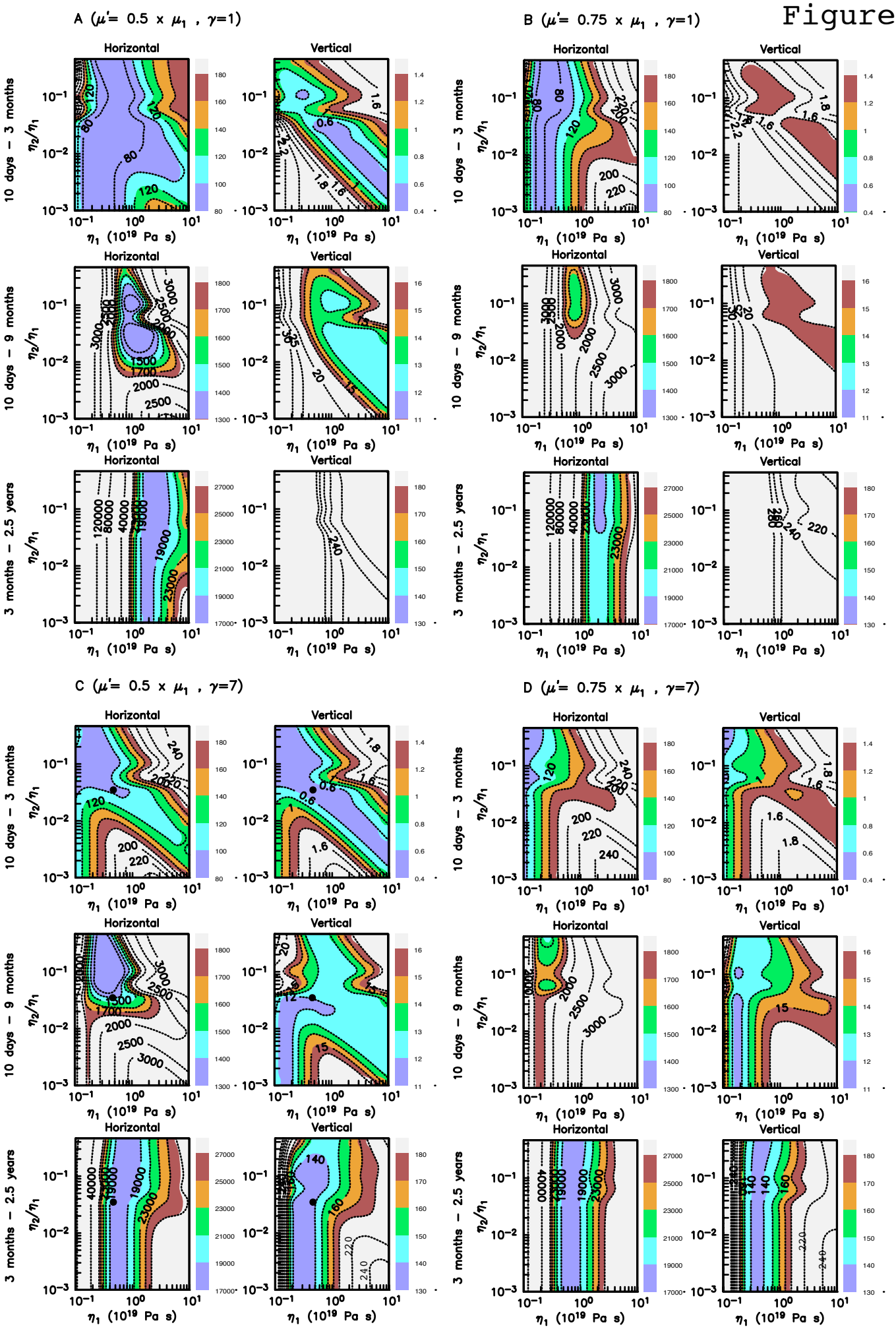
A (μ'= 0.5 x μ_1 , γ=1)
B (μ'= 0.75 x μ_1 , γ=1)
C (μ'= 0.5 x μ_1 , γ=7)
D (μ'= 0.75 x μ_1 , γ=7)
Horizontal
Vertical
10 days – 3 months
10 days – 9 months
3 months – 2.5 years
η_2/η_1
η_1 (10^{19} Pa s)

Figure 6

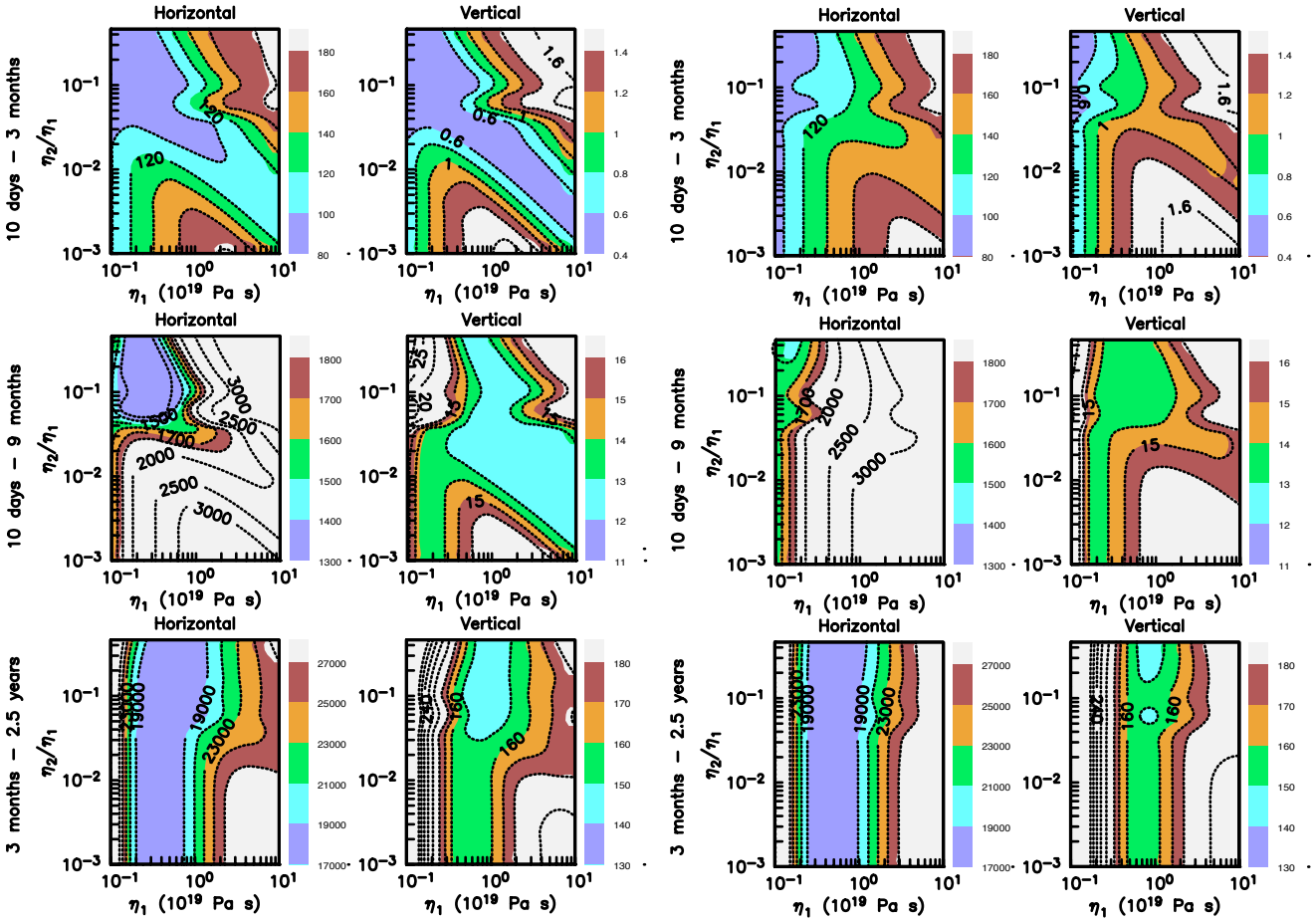
E (μ'= 0.5 x μ_1 , γ=20)
F (μ'= 0.75 x μ_1 , γ=20)
Horizontal
Vertical
10 days – 3 months
10 days – 9 months
3 months – 2.5 years
η_2/η_1
η_1 (10^{19} Pa s)

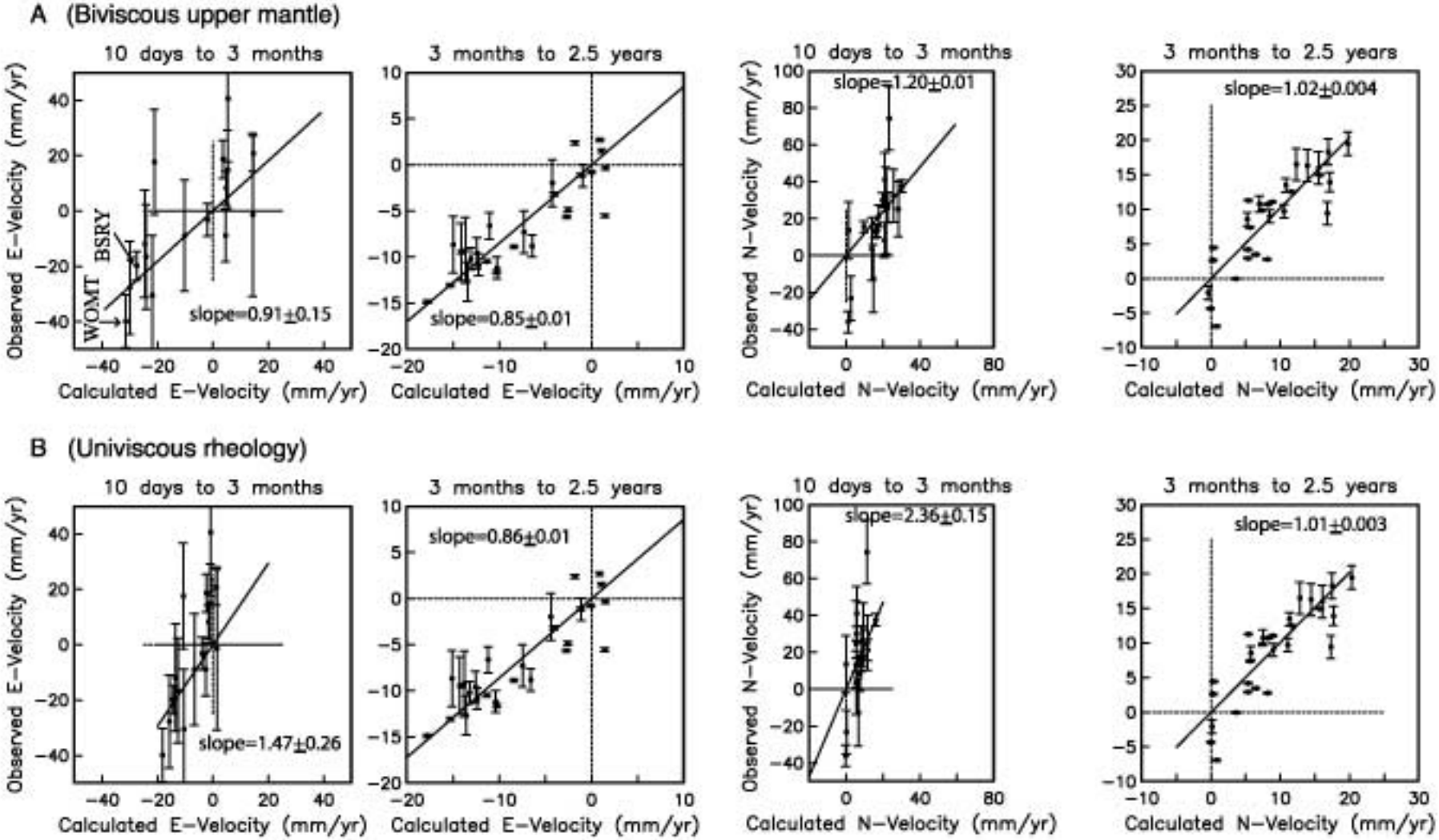
A (Biviscous upper mantle)
10 days to 3 months
3 months to 2.5 years
10 days to 3 months
3 months to 2.5 years
Observed E−Velocity (mm/yr)
Calculated E−Velocity (mm/yr)
Observed N−Velocity (mm/yr)
Calculated N−Velocity (mm/yr)
WOMT
BSRY
slope=0.91±0.15
slope=0.85±0.01
slope=1.20±0.01
slope=1.02±0.004
B (Univiscous rheology)
slope=1.47±0.26
slope=0.86±0.01
slope=2.36±0.15
slope=1.01±0.003

Figure 7

Figure 8

A (Biviscous upper mantle)

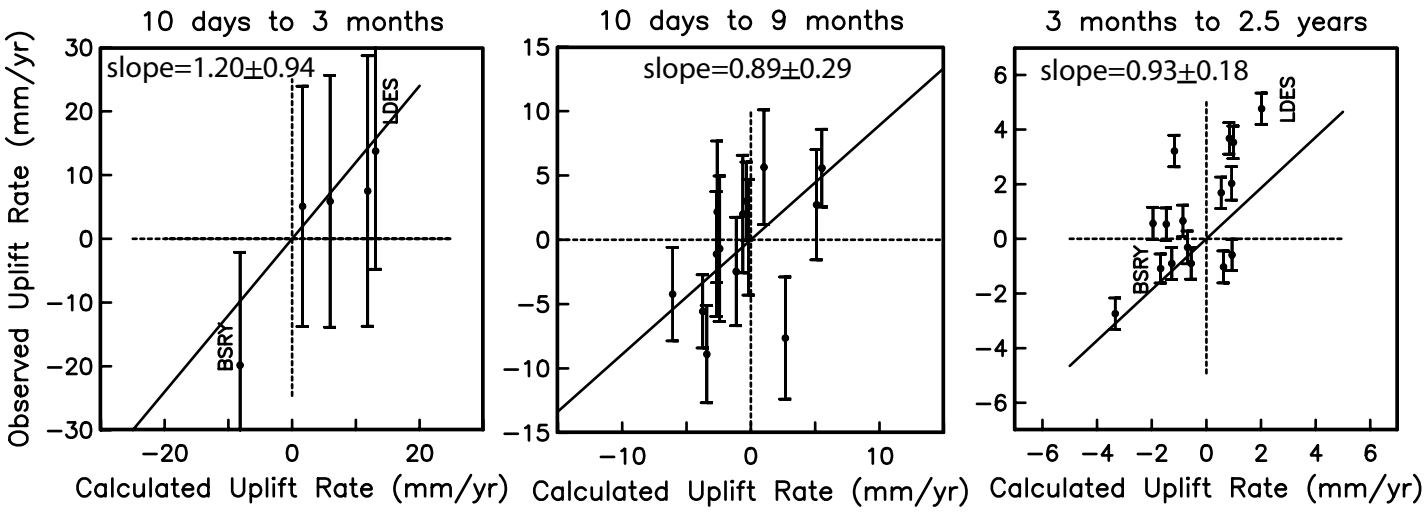

B (Biviscous lower crust)

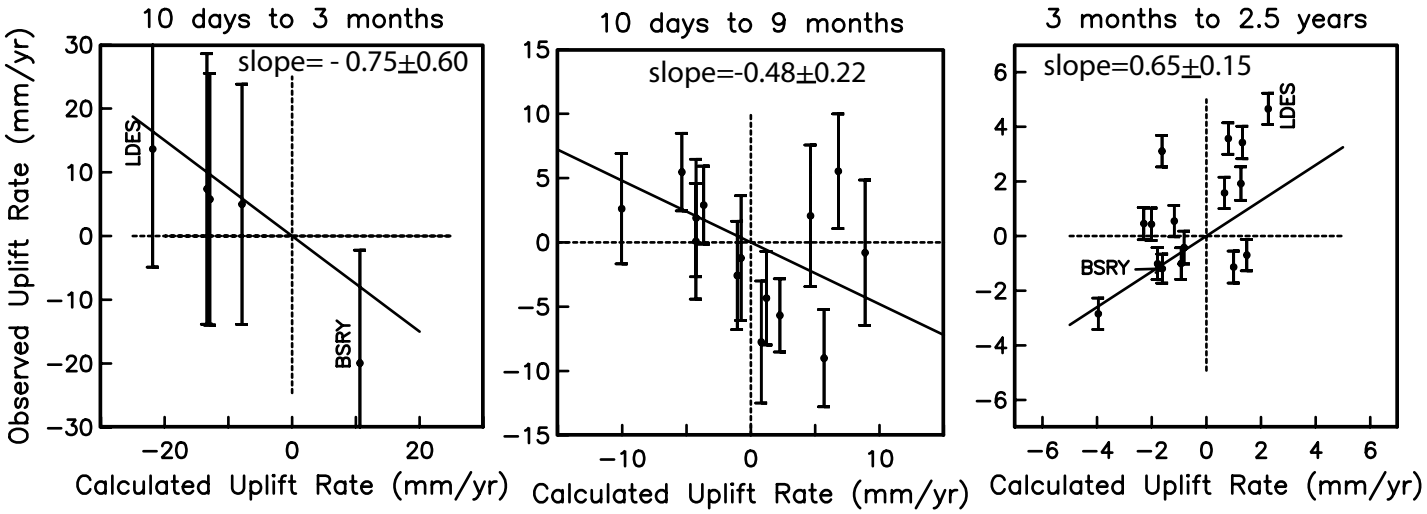

C (Afterslip model)

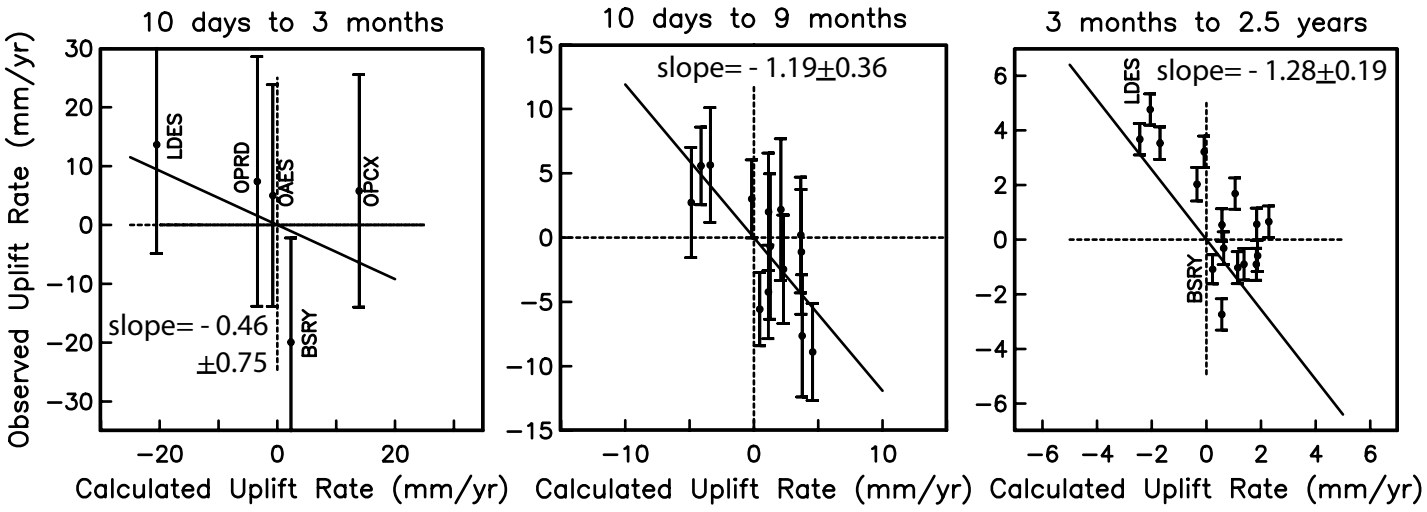

Figure 9

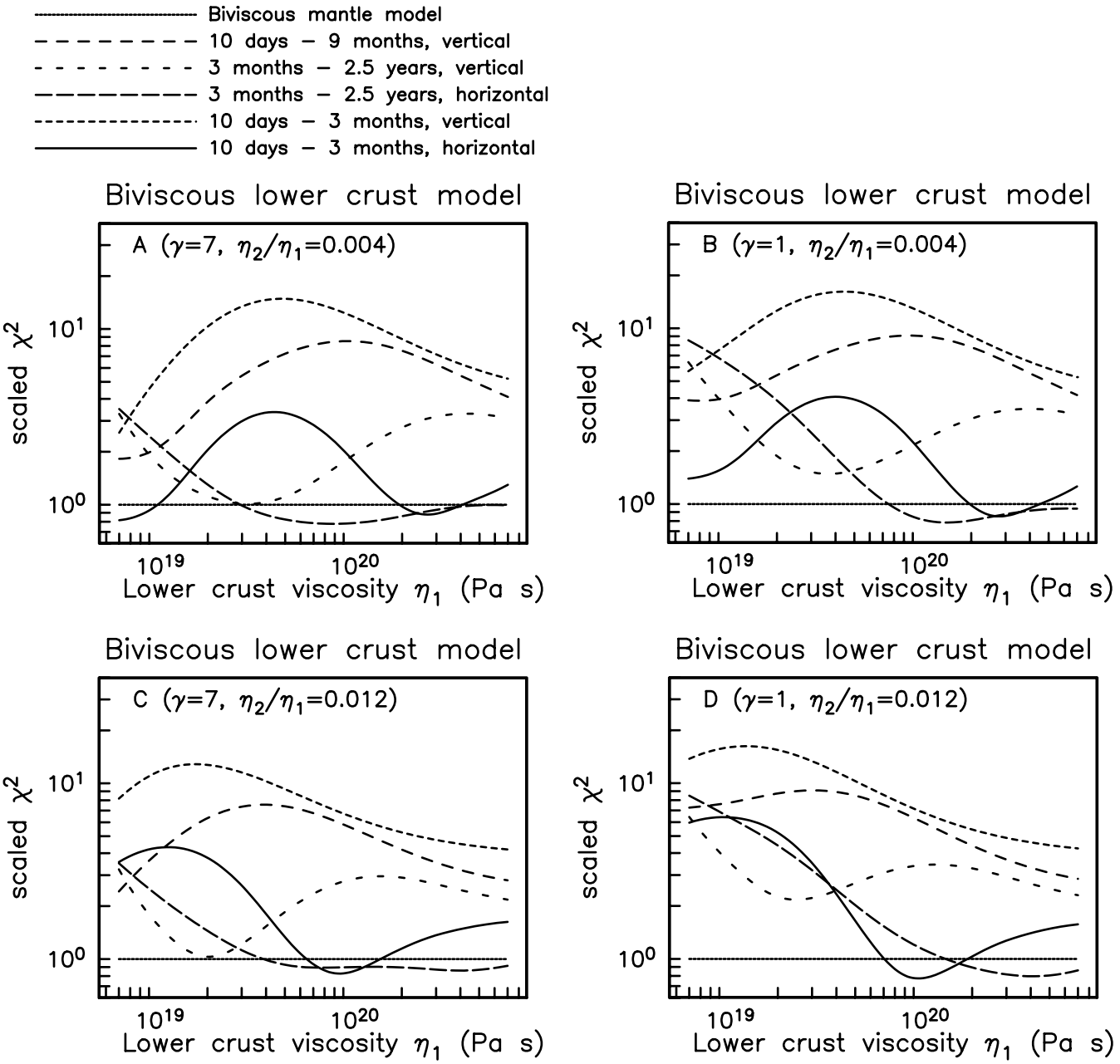
Biviscous mantle model
10 days – 9 months, vertical
3 months – 2.5 years, vertical
3 months – 2.5 years, horizontal
10 days – 3 months, vertical
10 days – 3 months, horizontal
Biviscous lower crust model
A (γ=7, η2/η1=0.004)
B (γ=1, η2/η1=0.004)
C (γ=7, η2/η1=0.012)
D (γ=1, η2/η1=0.012)
scaled χ2
10^1
10^0
10^19
10^20
Lower crust viscosity η1 (Pa s)

Figure 10

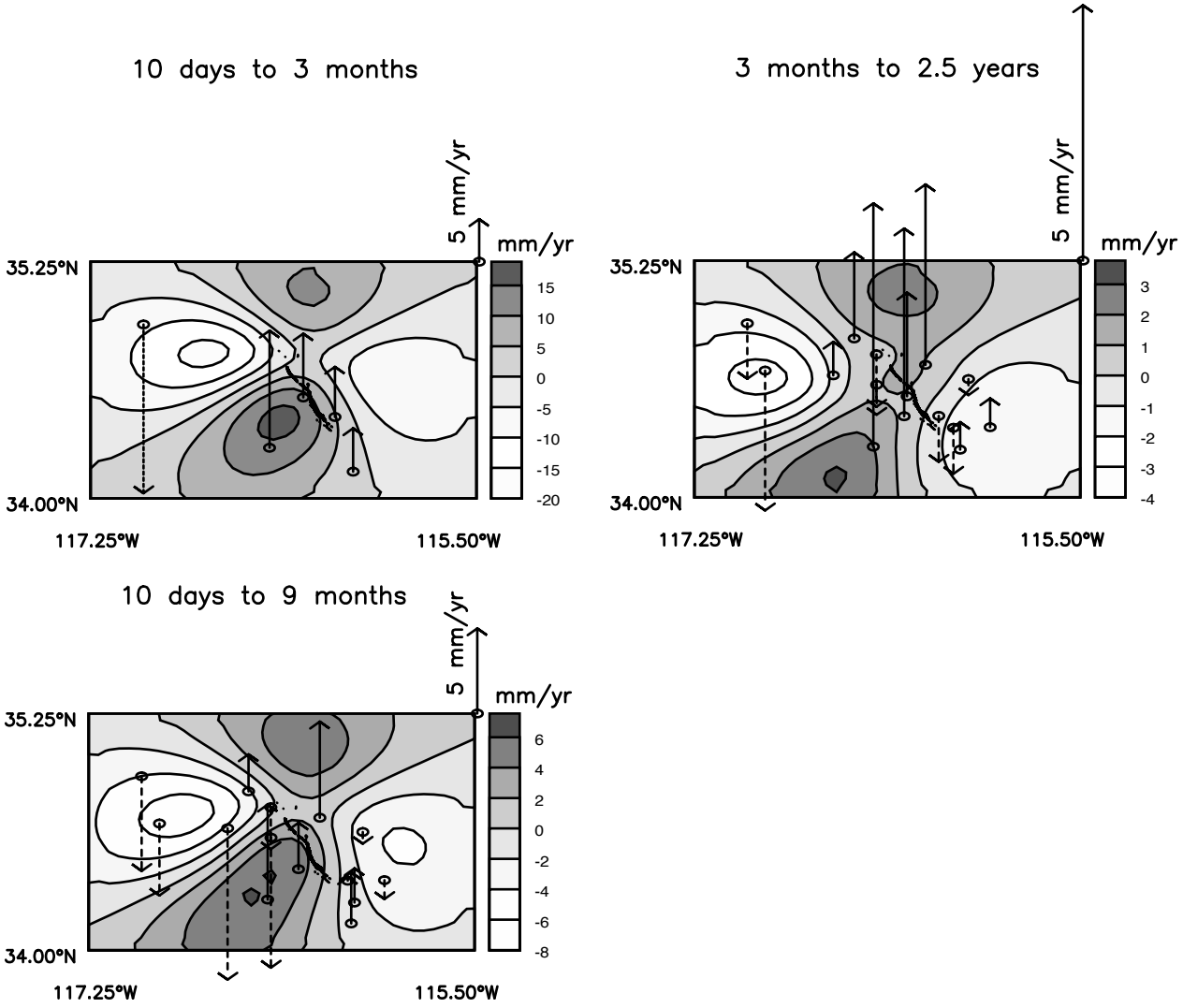
10 days to 3 months
5 mm/yr
mm/yr
15
10
5
0
-5
-10
-15
-20
35.25°N
34.00°N
117.25°W
115.50°W
3 months to 2.5 years
5 mm/yr
mm/yr
3
2
1
0
-1
-2
-3
-4
35.25°N
34.00°N
117.25°W
115.50°W
10 days to 9 months
5 mm/yr
mm/yr
6
4
2
0
-2
-4
-6
-8
35.25°N
34.00°N
117.25°W
115.50°W